ADVANCED MATERIALS
www.advmat.de

Highly Reliable Textile-Type Memristor by Designing Aligned Nanochannels

Yue Liu, Xufeng Zhou, Hui Yan, Xiang Shi, Ke Chen, Jinyang Zhou, Jialin Meng, Tianyu Wang, Yulu Ai, Jingxia Wu, Jiaxin Chen, Kaiwen Zeng, Lin Chen, Yahui Peng, Xuemei Sun, Peining Chen,* and Huisheng Peng**

Information-processing devices are the core components of modern electronics. Integrating them into textiles is the indispensable demand for electronic textiles to form close-loop functional systems. Memristors with crossbar configuration are regarded as promising building blocks to design woven information-processing devices that seamlessly unify with textiles. However, the memristors always suffer from severe temporal and spatial variations due to the random growth of conductive filaments during filamentary switching processes. Here, inspired by the ion nanochannels across synaptic membranes, a highly reliable textile-type memristor made of Pt/CuZnS memristive fiber with aligned nanochannels, showing small set voltage variation (<5.6%) under ultralow set voltage (≈0.089 V), high on/off ratio (≈10^6), and low power consumption (0.1 nW), is reported. Experimental evidence indicate that nanochannels with abundant active S defects can anchor silver ions and confine their migrations to form orderly and efficient conductive filaments. Such memristive performances enable the resultant textile-type memristor array to have high device-to-device uniformity and process complex physiological data like brainwave signals with high recognition accuracy (95%). The textile-type memristor arrays are mechanically durable to withstand hundreds of bending and sliding deformations, and seamlessly unified with sensing, power-supplying, and displaying textiles/fibers to form all-textile integrated electronic systems for new generation human-machine interactions.

1. Introduction

The emerging technologies like Internet of Things and fifth-generation mobile communiction have boosted the development of electronic textiles that are flexible and breathable like normal fabric, and they are considered as the ultimate form of wearables to revolutionize human-machine interaction paradigms.[1,2] Electronic textiles with functions of energy harvesting/storing,[3,4] sensing,[5,6] and displaying[7] have been created by interweaving optoelectronic fibers. For practical applications of electronic textiles, information processing device is the core building block to integrate functional electronic components together to form close-loop smart system.[8] However, traditional information processing devices with rigid substrate and multilayer structure hardly meet flexible, lightweight, and breathable demands of electronic textiles.[9] With the increasing mass of data produced in electronic textiles, it is critical while challenging to design robust woven information processing devices to seamlessly fit the interwoven structure and complex deformations of textiles.

Y. Liu, X. Zhou, X. Shi, K. Chen, J. Zhou, Y. Ai, J. Wu, K. Zeng, X. Sun, P. Chen, H. Peng
State Key Laboratory of Molecular Engineering of Polymers
Department of Macromolecular Science and Laboratory of Advanced Materials
Fudan University
Shanghai 200438, China
E-mail: peiningc@fudan.edu.cn; penghs@fudan.edu.cn

H. Yan, Y. Peng
School of Electronic and Information Engineering
Beijing Jiaotong University
Beijing 100044, China

J. Meng, T. Wang, L. Chen
State Key Laboratory of ASIC and System
School of Microelectronics
Fudan University
Shanghai 200433, China
E-mail: linchen@fudan.edu.cn

J. Chen
Department of Materials Science
Fudan University
Shanghai 200433, China

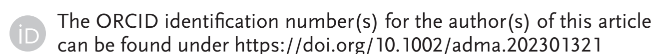
The ORCID identification number(s) for the author(s) of this article can be found under https://doi.org/10.1002/adma.202301321

DOI: 10.1002/adma.202301321

 © 2023 Wiley-VCH GmbH

Memristors with efficient in-memory computing capacity have typical crossbar configurations, which are inherently compatible with the interwoven structure of textiles,[10–12] and thus standing out as promising components to make flexible information processing textiles by weaving memristive fibers. However, the practical applications of memristors have long been hampered by unavoidable cycle-to-cycle and device-to-device variations during filamentary switching processes.[13–15] Such temporal and spatial variations generally result from the random growth of conductive filaments due to uncontrollable ion migrations in the amorphous memristive medium containing randomly distributed active defects.[16–18] Extensive efforts have been made to localize the active defects by inserting additional layer[19,20] and doping conductive impurities[21,22] in the memristive mediums, but the randomness of ion migration remains a common experience since active defects in an amorphous phase are intrinsically dynamic and unrestricted.[23] Although using single-crystal memristive materials with few defects could promote the reliability of resistive switching, it comes at great sacrifice of memristive performance.[24,25] Therefore, realizing highly reliable planar memristors remains an unmet need, let alone obtaining such robust textile-type memristors since it is particularly difficult to regulate memristive layer on the curved surface of micron-sized fiber electrodes.

In the biological neurons, aligned ion nanochannels with specific active sites across the synaptic membrane function as confined pathways to induce reliable and efficient transmembrane ion migrations,[26,27] thus allowing for robust electrical signal communications in neural network (**Figure 1**a). If such nanochannels decorated with active sites are created across memristive layer on the fiber electrode (Figure 1b), they may offer confined spaces for controllable ion migrations, and enable textile-type memristors with high reliability. Confining the growth of conductive filaments in several planar memristors was found to offer reproducible resistive switching based on modified vapor deposition methods,[28,29] but the vapor deposition with high temperature and vacuum conditions is inapplicable to fiber substrates for uniform and continuous memristive nanolayer.[12]

Here, we present such highly reliable textile-type memristors by depositing memristive CuZnS film with aligned nanochannels on Pt fiber electrodes. The nanochannels with abundant active S defects were created and regulated through chemical bath deposition method. The resultant textile-type memristors exhibited a four-fold reduction of set voltage (≈0.089 V), ten-fold reduction of set voltage variation (<5.6%) and 40-fold reduction of V_{set} standard deviation (≈0.005 V), compared with the counterparts without nanochannels in the CuZnS layer. The achieved reliability and memristive performances are superior to the typical planar filamentary memristors made of metal oxide, transition-metal chalcogenides, perovskites, and organic materials. The nanochannels with abundant active S defects were shown to anchor silver ions and confine their migrations to form orderly and efficient conductive filaments. Our textile-type memristors without any encapsulation in the array showed high device-to-device uniformity and were mechanically stable to withstand various deformations, so they can be seamlessly integrated into all-textile integrated electronic systems.

2. Results and Discussion

We chose CuZnS nanosheet as the memristive medium due to its high ionic mobility, structural adjustability, and stability.[30] Through the use of a chemical bath deposition method that is low-cost, scalable, and suitable for various substrates (Figure S1, Supporting Information), uniform and continuous CuZnS film with nanochannels was successfully deposited onto the curved surface of metal fiber electrodes ranging from tens to hundreds of micrometers in diameter. The prepared Pt/CuZnS fibers could be interlaced with metal fiber electrodes (e.g., Ag fiber) to obtain textile-type memristors, where each interlaced point between Pt/CuZnS and Ag fibers functioned as an individual memristor unit (Figure 1c,d).

In a typical preparation of Pt/CuZnS fibers, Pt fiber electrodes were first immersed in the precursor solution containing ethylene diamine tetraacetic acid (EDTA), $CuSO_4$ and $Zn(CH_3COO)_2$. After adding thioacetamide solution, S^{2-} reacted with Cu^{2+} and Zn^{2+} to form CuZnS film on the fiber electrode (Figure S2a,b, Supporting Information). Characteristic peaks of CuZnS were detected by X-ray diffraction spectroscopy (Figure S3, Supporting Information). Although CuS phases were formed in the CuZnS film, the electrical conductivity of CuZnS film was low because the content of CuS was low (Figure S2c–f, Supporting Information). In the deposition process, $EDTA^{2-}$ served as complexing agent to coordinate with Cu^{2+} and Zn^{2+}, thus controlling the aggregation rate of free ions in bulk solution.[31,32] The CuZnS film with nanochannels was then formed due to the drastic and disordered precipitation of aggregations according to the mechanism of homogeneous growth[33,34] (Figure S4, Supporting Information). Specifically, dense CuZnS film without nanochannels was formed as the EDTA/precursor ratio was 0.28 (Figure S5, Supporting Information), while uniform nanochannels with sizes of 17.4 ± 4 nm were formed as EDTA/precursor ratio was 0.2 (Figure 1e; Figures S6a and S7, Supporting Information). Moreover, the nanochannels also showed uniform size distribution at different positions along the Pt/CuZnS fiber (Figure S6b, Supporting Information). The nanochannels with larger sizes (e.g., ≈50 and ≈200 nm) could be achieved by further decreasing EDTA/precursor ratios (Figure S8, Supporting Information).

The fine structures and mechanical properties of CuZnS film containing nanochannels (with EDTA/precursor ratio of 0.2) were carefully characterized. Atomic force microscopy image indicated the nanochannels had a similar average depth with the thickness of CuZnS film (≈50 nm) from cross-sectional images (Figures S9 and S10, Supporting Information). These nanochannels were perpendicular to the fiber substrate (Figure 1e). Such vertical arrangement was also verified by the 2D grazing incidence small-angle X-ray scattering (GISAXS) (Figure 1f), in which two spots were symmetrically distributed around the grazing incidence X-ray beam. Transmission electron microscope (TEM) image showed that amorphous phase of CuZnS decorated around the nanochannel was formed in the crystalline phase, which probably originated from the phase transition during the reaction and post-treatment processes[35] (Figure 1g; Figure S11a, Supporting Information). Such amorphous/crystalline heterogeneous structure was further verified by the selected area electron diffraction pattern with coexistence of weak amorphous halo and

 © 2023 Wiley-VCH GmbH

15214095, 2023, 32, Downloaded from https://onlinelibrary.wiley.com/doi/10.1002/adma.202301321 by Fudan University, Wiley Online Library on [12/12/2024]. See the Terms and Conditions (https://onlinelibrary.wiley.com/terms-and-conditions) on Wiley Online Library for rules of use; OA articles are governed by the applicable Creative Commons License

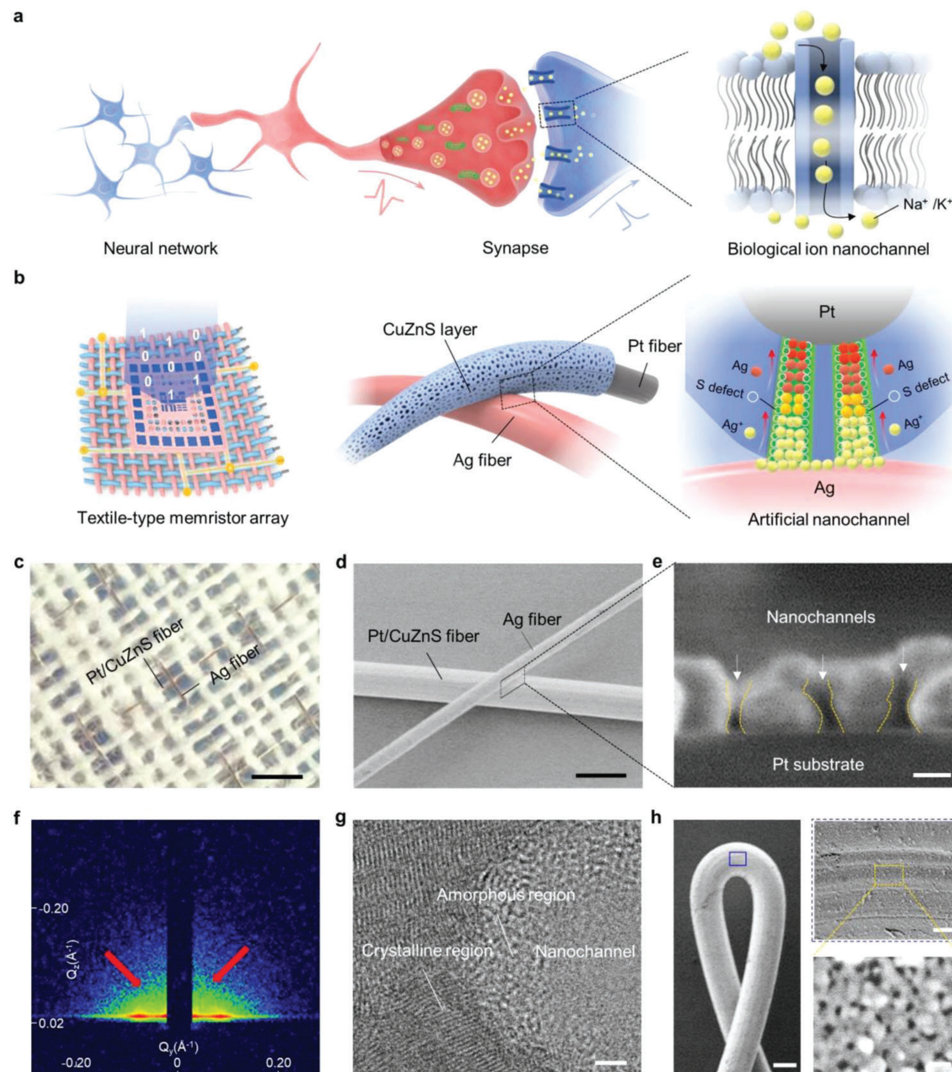

Figure 1. Design and structural characterization of textile-type memristor made of nanochannels-contained Pt/CuZnS fiber. a) Schematic showing biological neural network that transfers and processes electrical signals between pre-neurons and post-neurons. Biological nanochannels across the synaptic membrane function as confined pathways to induce orderly and fast transmembrane ion migration. b) Schematic showing textile-type memristor woven with Pt/CuZnS fibers and Ag fiber electrodes (left and middle). Nanochannels decorated with active sites in the CuZnS film provide confined space for ion migration and growth of conductive filament upon applying voltage (right). c) Photograph of the textile-type memristor. Each interlaced point between Pt/CuZnS fibers and Ag fiber electrodes functions as an individual memristor unit. Scale bar, 2.0 mm. d) SEM image of a textile-type memristor unit by interlacing Pt/CuZnS fiber (50 µm) and Ag fiber electrodes (20 µm). Scale bar, 50 µm. e) Cross-sectional SEM image of CuZnS film on the Pt fiber electrode. Vertical nanochannels were formed across the CuZnS film. Scale bar, 50 nm. f) GISAXS image of CuZnS film with nanochannels showing two obvious spots (marked with red arrows). g) High-resolution TEM image of the nanochannel. Amorphous phase of CuZnS decorated around the nanochannel was formed in the crystalline phase. Scale bar, 2 nm. h) SEM image of a Pt/CuZnS fiber being bent with a curvature radius of 0.1 mm. No obvious peeling of CuZnS layer (left) was observed. Enlarged views show no obvious cracks (top right) and damages of nanochannels (bottom right) occurred. Scale bars, 30 µm (left), 1 µm (top right), and 60 nm (bottom right).

sharp crystalline reflections (Figure S11b, Supporting Information). These nanochannels featured with heterogeneous structure across the CuZnS film are expected to provide predefined pathways for efficient and orderly ion migrations and growth of conductive filaments. Furthermore, the CuZnS film on the Pt fiber electrode was mechanically robust to withstand various deformations. For instance, when the Pt/CuZnS memristive fiber was sharply bent with curvature radii from 1.5 to 0.1 mm (Figure 1h; Figures S12 and S13, Supporting Information), the nanochannels on the CuZnS layer were well maintained, and even no obvious peeling or delamination of the interface occurred upon bending with a curvature radius of 0.1 mm. Such structural stability might originate from the mechanical stiffness of CuZnS film (Figure S14, Supporting Information), and is crucial for the performing stability of resultant textile-type memristors under complex deformations in the wearable uses.

The prepared Pt/CuZnS fiber was interlaced with Ag fiber electrode to form a memristor unit (with area of ≈270 µm^2, **Figure 2**a)

 © 2023 Wiley-VCH GmbH

15214095, 2023, 32, Downloaded from https://onlinelibrary.wiley.com/doi/10.1002/adma.202301321 by Fudan University, Wiley Online Library on [12/12/2024]. See the Terms and Conditions (https://onlinelibrary.wiley.com/terms-and-conditions) on Wiley Online Library for rules of use; OA articles are governed by the applicable Creative Commons License

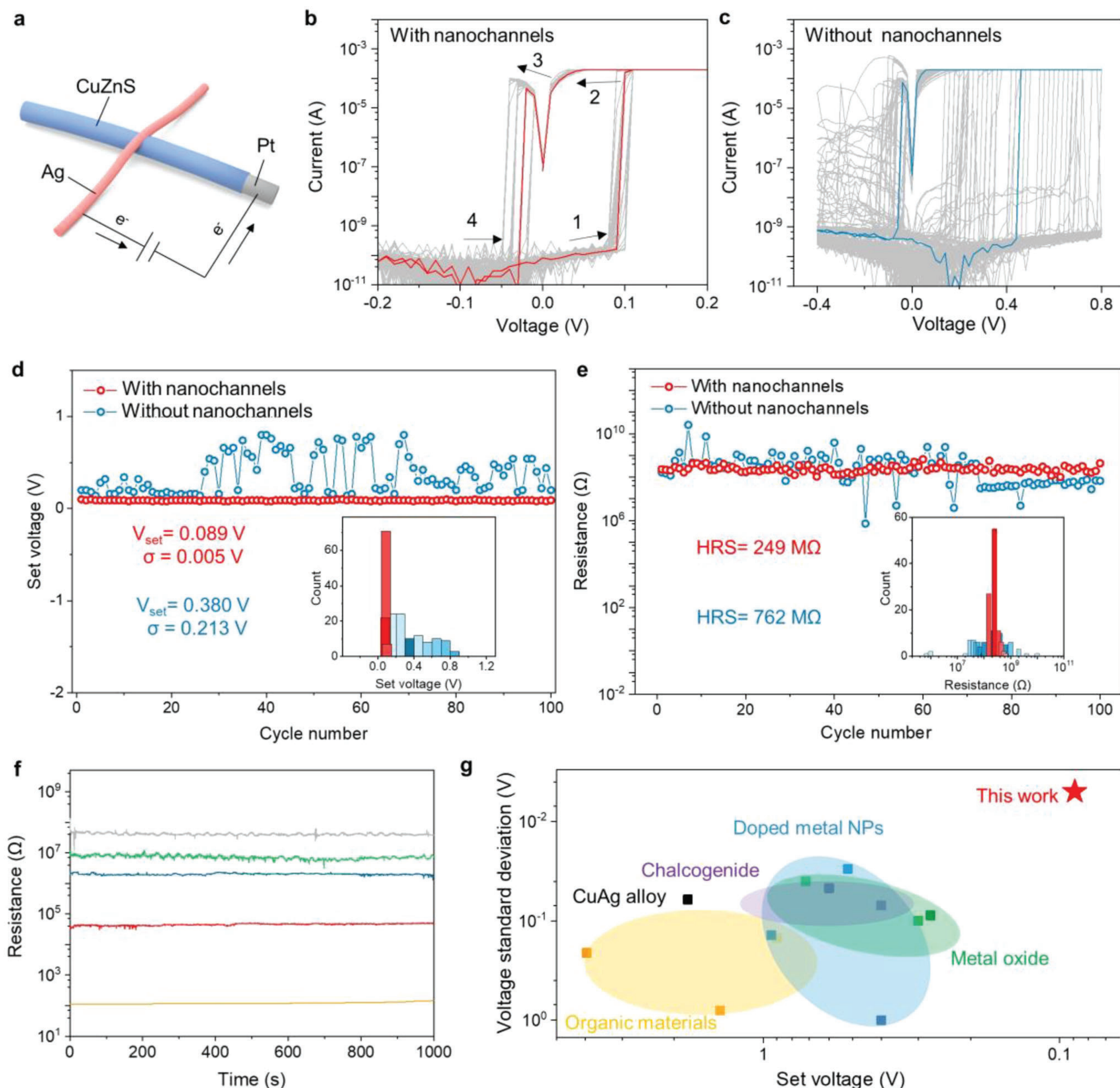

Figure 2. Memristive performances of textile-type memristors. a) Schematic to demonstrate the working process of a textile-type memristor. The Ag fiber electrode was applied by a voltage, while the Pt/CuZnS fiber was connected to the ground. b,c) Current–voltage (*I*–*V*) curves of textile-type memristor units with and without nanochannels, respectively. *I*–*V* curves show typical nonvolatile bipolar resistive switching behavior. d) Variation of set voltages in the investigated 100 switching cycles for textile-type memristor unit made of Pt/CuZnS fiber. Histograms (inset) show memristor unit with nanochannels has more narrowly distributed set voltages than that without nanochannels. σ is the standard deviation of set voltage. e) Resistance variation of high resistance state (HRS) during 100 switching cycles for the memristor unit made of Pt/CuZnS fibers. Histograms (inset) show the memristor with nanochannels has more narrowly distributed HRS than that without nanochannels. f) The retention of multilevel resistance states for the memristor with nanochannels. g) Comparison of the set voltage and standard variation between nanochannel-contained memristor and state-of-the-art planar filamentary memristors.

that integrated with interwoven structure of textile. The resistive switching behavior of such textile-type memristor unit was investigated by applying direct voltage sweep on the Ag fiber electrode. For the textile-type memristor unit bearing nanochannels (with an average size of ≈17 nm) in the CuZnS layer, it demonstrated a typical nonvolatile bipolar resistive switching behavior from the continuous current–voltage (*I*–*V*) curves (Figure 2b), and no obvious electroforming process occurred in the first switching cycle. As the average size of nanochannels increased from 17 to 50 nm, the textile-type memristor unit showed larger fluctuations both in set voltage and resistance state; it even completely collapsed in the initial switching cycles as the nanochannel size

© 2023 Wiley-VCH GmbH
15214095, 2023, 32, Downloaded from https://onlinelibrary.wiley.com/doi/10.1002/adma.202301321 by Fudan University, Wiley Online Library on [12/12/2024]. See the Terms and Conditions (https://onlinelibrary.wiley.com/terms-and-conditions) on Wiley Online Library for rules of use; OA articles are governed by the applicable Creative Commons License

further enlarged to 200 nm (Figures S15 and S16, Supporting Information). Unless otherwise specified, the memristor with an average nanochannel size of ≈17 nm was used in the following study.

The memristive behaviors of textile-type memristors made of Pt/CuZnS fibers with and without nanochannels were systemically compared. In comparison to textile-type memristor without nanochannels, the textile-type memristor with nanochannels exhibited much lower and more reliable set voltages with a slight fluctuation (from 0.08 to 0.11 V) during the investigated 100 switching cycles (Figure 2c). The average set voltage (≈0.089 V) for the textile-type memristor with nanochannels was ≈4 times lower than that (≈0.38 V) for the counterpart without nanochannels, and even far lower than the available planar filamentary memristors (typically 0.5 V, Table S1, Supporting Information). Such switching reliability was further verified by the statistical analysis of set and reset voltages in the investigated 100 switching cycles (Figure 2d; Figure S17a, Supporting Information). The standard deviation of set voltages (≈0.005 V) and set voltage variation (namely $V_{\text{set s.d}}/V_{\text{set average}}$, 5.6%)[22] were ≈40 and ≈10 times lower than those (≈0.213 V and 56.1%) without nanochannels, respectively. The resistance values of both high-resistance state (HRS) and low-resistance state (LRS) for the memristor unit with nanochannels were also well maintained over 100 switching cycles, compared with the large fluctuations of HRS and LRS for the counterpart without nanochannels (Figure 2e; Figures S17b and S18, Supporting Information); the HRS fluctuation for the former ($R_{\text{s.d}}/R_{\text{average}}$, 38.3%) was ≈9 times lower than that of the later (349%). The surface of fiber electrode remained smooth after cyclic switching (Figure S19, Supporting Information). Moreover, the memristor units showed stable resistance retention of over 1000 s under multiple distinguished resistance states (Figure 2f), the LRS was even well maintained after an extended retention of 40 000 s under a high temperature of 85 °C (Figure S20, Supporting Information).[21]

Overall, the textile-type memristor unit made of Pt/CuZnS fiber with nanochannels exhibited both ultralow set voltage (≈0.089 V) and set voltage variation (<5.6%). Compared with the overwhelming majority of available planar filamentary memristors, the textile-type memristor with nanochannels achieved the lowest set voltage and standard deviation of set voltages (Figure 2g). For instance, the set voltage of the textile-type memristor was ≈5 times lower than that of typical metal-oxide memristors; the standard deviation of set voltage was ≈9 times lower than that for the typical chalcogenide memristors. Additionally, the set voltage of the textile-type memristor was ≈400 times lower than that of the reported planar memristors with confined channels, combined with a comparable variation of set voltage. The textile-type memristor could be switched within 30 ns with low energy consumption of ≈3.7 pJ and power consumption of ≈0.1 nW (Figure S21, Supporting Information), which is comparable to the state-of-the-art planar filamentary memristors (Table S1, Supporting Information). Moreover, the high on/off ratio (≈10^6) is helpful to alleviate the crosstalk and noise issue in the array-level application. As expected, the achieved ultralow set voltage and high switching reliability could significantly reduce the design complexity and peripheral overheads of textile-type memristor array and facilitate efficient information processing in textile-type electronic system.

In principle, the resistive switching behaviors of filamentary memristor greatly depend on the ion migration and growth of conductive filament in the memristive layer, which is generally determined by the local nanostructures and chemical environments.[36–38] Based on the above experimental results, we attributed the ultralow set voltage and switching reliability to the nanochannels with amorphous/crystalline heterostructures across the CuZnS layer (**Figure 3**a). Specifically, as a voltage is applied on the fiber electrodes, assisted by the active defect sites in amorphous region of CuZnS inside the nanochannels, Ag^+ generated at the surface of Ag electrode will preferentially move toward Pt electrode along the nanochannels. Orderly conductive silver filaments are thus formed in the confined space of nanochannels after reduction of Ag^+, thus enabling memristors to switch with ultralow set voltage and high reliability.

We first performed finite element simulation to investigate the electric field distribution in the CuZnS film with nanochannels (Figure 3b). An obvious electric field enhancement was formed at the nanochannels adjacent to the Ag fiber electrode. Kelvin probe force microscopy further experimentally displayed an obvious electronic potential well at the nanochannels (Figure S22, Supporting Information).[39] Such electric field enhancement could promote preferential generation and migration of Ag^+ in the nanochannels. X-ray photoelectron spectroscopy analysis was then performed to understand the local chemical environment in the nanochannels. Compared with CuZnS film without nanochannels, the nanochannel-contained CuZnS film showed obvious negative shifts of S $2p_{3/2}$ (from 162.1 to 161.2 eV) and S $2p_{1/2}$ (from 169.1 to 168.6 eV) (Figure 3c), indicative of S defects generation.[40,41] Such S defects were also verified by the low-energy shifting of Cu K-edge from X-ray absorption near edge structure spectra (Figure S23, Supporting Information),[41,42] and the generation of sharp electron paramagnetic resonance signal (g = 2.0032) (Figure S24, Supporting Information). Aberration-corrected scanning transmission electron microscopy further indicated S defects might locate at amorphous and grain boundary around the nanochannels (Figure S25, Supporting Information). The lower slope of Mott–Schottky curve for nanochannel-contained CuZnS film than that of counterpart without nanochannels indicated the higher carrier density (Figure 3d), which could enhance Ag^+ mobility and diffusion kinetics.[43,44] By fitting the representative *I*–*V* curve of nanochannel-contained memristor, its resistive switching behavior followed a typical space charge limited mode (Figure 3e),[45] indicating that the active S defects indeed played a crucial role in Ag^+ migration.

To understand the interaction of Ag^+ with active S defects, we carried out XPS measurements of the interfacial region between CuZnS film and Ag electrode during the resistive switching process. When the set voltage increased from 0 to 0.1 V (the resistive switching point), with the generation of Ag^+ (indicated by the enhancement of 3*d* peak of Ag and the increase of atomic percentage of Ag from 0.01 to 0.23) (Figure 3f; Table S2, Supporting Information), the S $2p_{1/2}$ peak obviously shifted to the higher binding energy, accompanied with the shoulder peak of S $2p_{3/2}$ (Figure 3g), indicating that Ag^+ was bound to active S defects in the nanochannels. That is, active S defects were capable of anchoring Ag^+ to promote its migration along the nanochannels for the growth of orderly Ag filament. The density functional theory

© 2023 Wiley-VCH GmbH

15214095, 2023, 32, Downloaded from https://onlinelibrary.wiley.com/doi/10.1002/adma.202301321 by Fudan University, Wiley Online Library on [12/12/2024]. See the Terms and Conditions (https://onlinelibrary.wiley.com/terms-and-conditions) on Wiley Online Library for rules of use; OA articles are governed by the applicable Creative Commons License

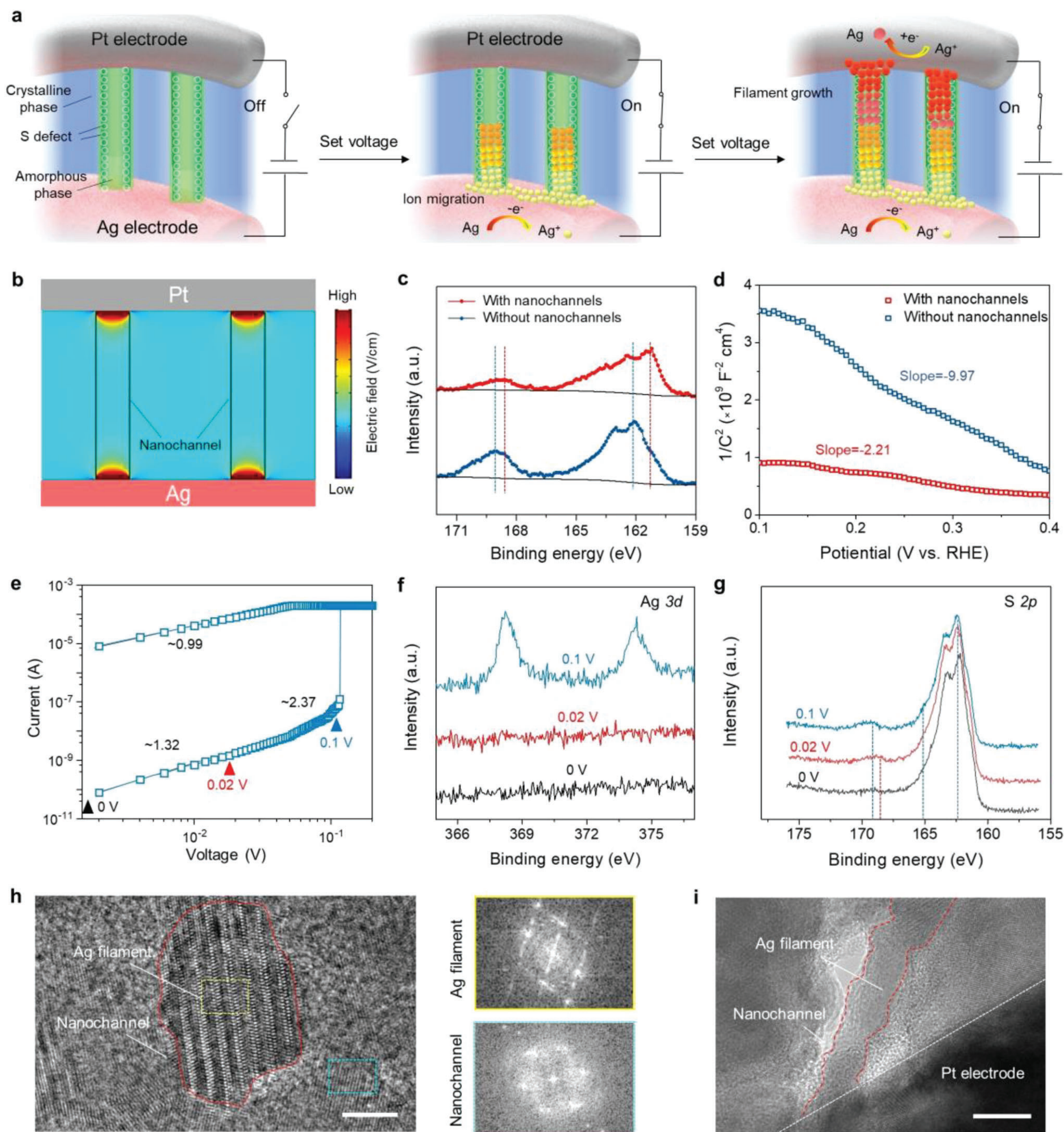

Figure 3. Resistive switching mechanism of textile-type memristor made from nanochannel-contained CuZnS film. a) Schematic illustrations of proposal switching mechanism. The nanochannels confined ion migrations along the nanochannels by the active S defects in the amorphous region of CuZnS (left and middle), thus enabling orderly and efficient growth of Ag filament (right). b) Finite element simulation of electric field distribution in the CuZnS film with nanochannels under applied voltage. Local enhancement of electric field is formed at the nanochannels. c) XPS spectra of S 2*p* for CuZnS film with nanochannels showing a negative shift to low binding energy compared with that without nanochannels. d) Mott–Schottky curve for CuZnS film with nanochannels showing a lower slope than that without nanochannels. e) Fitted *I*–*V* curve of nanochannel-contained memristor unit showing the resistive switching process followed a space charge limited mode. f,g) XPS spectra of f) Ag 3*d* and g) S 2*p* at the interfacial region between the nanochannels-contained CuZnS film and Ag electrode as the set voltage increased from 0, 0.02 to 0.1 V. h) High-resolution TEM (left) of nanochannels-contained CuZnS film showing Ag filament was formed in the nanochannel. The fast Fourier transform patterns show that Ag filament crystal structure (upper right) was different from the nanochannel (bottom right). Scale bar, 5 nm. i) Cross-sectional TEM image of the nanochannel embedded with Ag filament when the memristor was under the set state. Scale bar, 20 nm.

 © 2023 Wiley-VCH GmbH

15214095, 2023, 32, Downloaded from https://onlinelibrary.wiley.com/doi/10.1002/adma.202301321 by Fudan University, Wiley Online Library on [12/12/2024]. See the Terms and Conditions (https://onlinelibrary.wiley.com/terms-and-conditions) on Wiley Online Library for rules of use; OA articles are governed by the applicable Creative Commons License

15214095, 2023, 32, Downloaded from https://onlinelibrary.wiley.com/doi/10.1002/adma.202301321 by Fudan University, Wiley Online Library on [12/12/2024]. See the Terms and Conditions (https://onlinelibrary.wiley.com/terms-and-conditions) on Wiley Online Library for rules of use; OA articles are governed by the applicable Creative Commons License

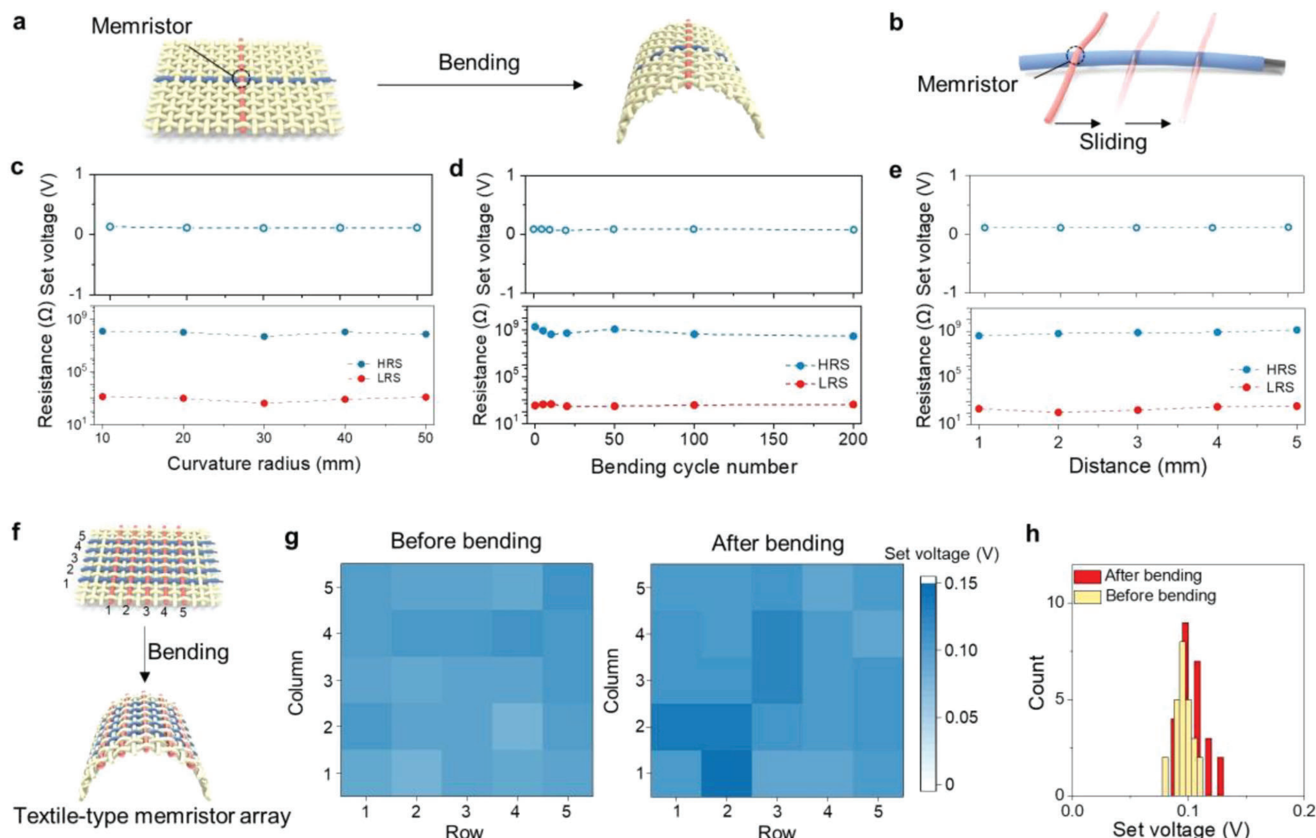

Figure 4. Reliability and durability of textile-type memristor under complicated deformations. a) Schematic showing the woven textile-type memristor unit to be bent. b) Schematic showing the Ag fiber electrode (red) of textile-type memristor slid to different positions on the Pt/CuZnS fiber. c,d) Variations of set voltage and resistance state of textile-type memristor as it was bent with c) different curvature radii and d) after bending cycles (curvature radius of 10 mm), respectively. e) Variations of set voltage and resistance state of textile-type memristor when Ag fiber electrode slid with different distances along the Pt/CuZnS fiber. f,g) Schematic showing a 5 × 5 f) textile-type memristor array and map of set voltages of 25 memristor units g) before and after 100 cycles of bending. h) Histogram of the spatial set voltage among the 5 × 5 textile-type memristor array in (g) showing high device-to-device uniformity before and after bending.

calculations showed that the energy barrier of surface migration for Ag ions with S defects was low enough to be readily overcome (Figures S25–S27, Supporting Information). Therefore, S defects around the nanochannels could provide preferential diffusion pathways for Ag ions to promote the growth of conductive filaments.[28,46,47] We also carried out TEM to verify the Ag filament confined in the nanochannels. As shown in the Figure 3h, the crystal phase with a lattice fringe of 0.24 nm in the nanochannel (surrounded by CuZnS crystal region) is consistent with the Ag (110) crystal face, indicating that Ag filaments were indeed formed and confined in the nanochannels. Such growth of Ag filament was also confirmed by the fast Fourier transform patterns (two typical regions), and cross-sectional TEM image of Ag filament embedded in the nanochannel (Figure 3i). According to the above analyses, we concluded that the nanochannels decorated with abundant active S defects across the CuZnS layer could anchor Ag^+ and accelerate their migration to form orderly and controllable conductive filaments, thus leading to reliable resistive switching under ultralow set voltage.

The textile-type memristors without encapsulation were durable to withstand various deformations like bending, sliding, pressing, stretching, and twisting (**Figure 4**a,b; Figure S28, Supporting Information), indicating the potential for wearable applications. When the textile-type memristor was bent with a wide range of curvature radii from 50 to 10 mm (Figure 4c), and even repeatedly bent for 200 cycles (with a curvature radius of 10 mm) (Figure 4d), the set voltage and resistances of HRS and LRS were well maintained.[48,49] Moreover, no obvious degradation of memristive performances occurred both as the Ag fiber electrode slid along the Pt/CuZnS fiber (Figure 4e), which was consistent with the fact that the surface of fiber electrode remained smooth after cyclic sliding (Figure S19, Supporting Information). Similarly, the resistance state and set voltage were maintained to be stable when the Pt/CuZnS fiber interlaced at different positions of Ag fiber electrode (Figure S29, Supporting Information). Such durability of textile-type memristors might originate from the both smooth and stable surface of fiber electrode and the robust interface between the Pt fiber electrode and CuZnS film under various deformations (Figures S19, S30, and S31, Supporting Information).

To evaluate the device-to-device uniformity of textile-type memristor for array-level applications, we weaved Pt/CuZnS fibers, Ag fibers and cotton yarns together to obtain a 5 × 5 textile-type memristor array (Figure 4f). The 25 memristor units

 © 2023 Wiley-VCH GmbH

15214095, 2023, 32, Downloaded from https://onlinelibrary.wiley.com/doi/10.1002/adma.202301321 by Fudan University, Wiley Online Library on [12/12/2024]. See the Terms and Conditions (https://onlinelibrary.wiley.com/terms-and-conditions) on Wiley Online Library for rules of use; OA articles are governed by the applicable Creative Commons License

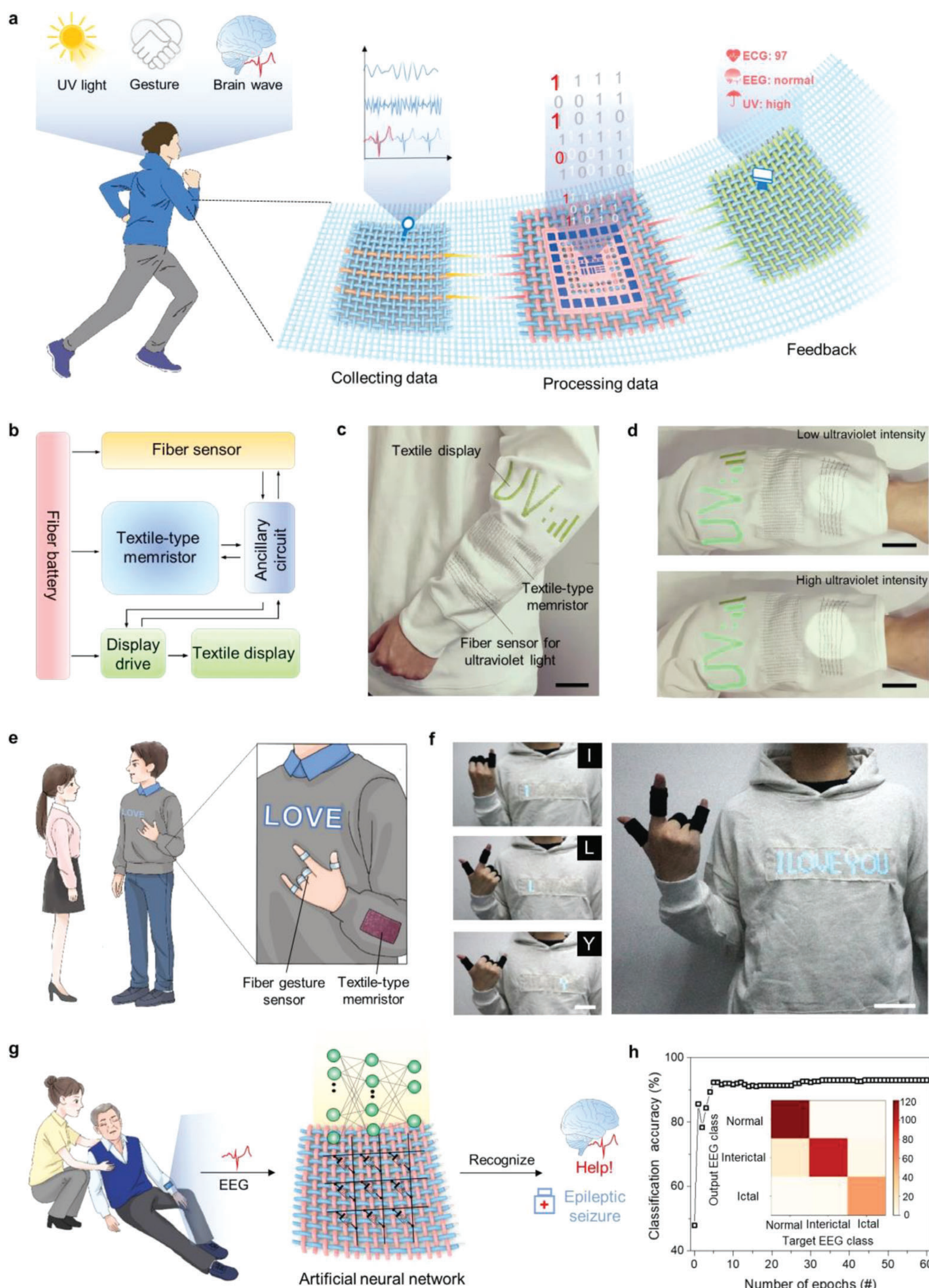

Figure 5. Applications of all-textile integrated electronic systems integrated with textile-type memristors. a) Schematic showing textile-type memristors integrated with sensing, power-supplying, and displaying modules to form all-textile electronic system for interactive applications. b) System-level block diagram of the all-textile electronic system. The sensing, power-supplying and displaying modules are connected to textile-type memristors with the assistance of ancillary circuit. c) Photograph of an ultraviolet-light-monitoring-feedback cloth consisting of textile-type memristors, ultraviolet light fiber sensor, and textile display. Scale bar, 5 cm. d) Real-time UV light monitor at the sleeve to alert ultraviolet light intensities. Scale bars, 5 cm. e) Schematic showing a smart cloth integrated with textile-type memristors and fiber triboelectric sensors. The gestures of people with language disorders were translated into voltages through triboelectric sensors worn on the fingers, which were further analyzed by textile-type memristors to feed back to textile display. f) Photographs showing the gestures of 'I Love You' were translated and displayed on the cloth through the all-textile electronic system. Scale bars, 8 cm. g) Schematic showing a real-time medical diagnosis textile system can recognize brain waves of "Normal", "Epileptic interictal phase", and "Epileptic ictal phase", collected from patients with epilepsy. h) Recognition accuracy for the EEG signals reached up to 95%. Inset: the confusion matrix for a classification test of EEG patterns showing that the diagonal tiles in the matrices are mostly saturated in red.

 © 2023 Wiley-VCH GmbH

showed a device yield of 100%, with slight variations of set voltage (<10%) and resistance states (Figure 4g; Figures S32 and S33, Supporting Information), benefitted from the uniform size distribution of nanochannels along the Pt/CuZnS fiber. In particular, no obvious degradation occurred among the memristor units even after the textile-type memristor array was bent for 100 cycles, the set voltage of each memristor unit was well maintained with an average variation of <10%, and the average set voltages of 25 memristor units before and after bending also varied by <10% (Figure 4h). Such resistive switching reliability, device uniformity and mechanical durability of textile-type memristor array were crucial to meet the wearable requirements for practical uses.[15,50,51] Moreover, the woven textile memristor showed good flexibility, breathability and moisture permeability like commercial clothing (Table S3, Supporting Information). With reduction in the diameter of fiber electrode, it is expected that high-density and large-scale textile memristor arrays can be fabricated through industrial weaving technologies.

As a proof-of-concept for applications, the textile-type memristors were seamlessly integrated with sensing, power-supplying and displaying textiles to obtain all-textile electronic system (**Figure 5**a). The auxiliary circuit and programmed algorithms could be introduced to address the non-idealities issue in memristor crossbar array.[52,53] Specifically, the physiological and environmental signals collected by sensors were directly processed by textile-type memristors and visually fed back through textile display, thus offering an effective and comfortable interactive tool. For instance, we fabricated an ultraviolet-light-monitoring-feedback cloth by weaving together textile-type memristors, fiber sensors for ultraviolet light detection and textile display (Figure 5b,c; Figure S34a–d, Supporting Information). When people outside were exposed to sunlight, the fiber sensors transformed the intensity of ultraviolet light into photocurrent. Then, the memristor judged whether the value of photocurrent exceeded the safe threshold according to the voltage division in series circuit,[54,55] and sent the result to the driver module for triggering the alarm signal on the textile display (Figure 5d; Figure S34e–h, Supporting Information). Such flexible and breathable smart cloth could remind us of real-time ultraviolet level for timely personal protection in outdoor activities. Similarly, the textile-type memristors could also be integrated with fiber triboelectric sensors (Figure S35, Supporting Information) to transform hand gestures of people with language disorders into visualized images for effective communications (Figure 5e). The finger-bending signals collected by triboelectric sensors worn on the finger joints were processed by the textile-type memristors woven at the sleeve, and finally gave feedback by visual display in textile such as "I Love You" (Figure 5f).

Benefiting from their robust memristive performances, the textile-type memristors could be made into large-scale array to function as artificial neural network for efficient classification and recognition of complex data in wearable use. To verify the data recognition ability of textile-type memristor array, a three-layer neural network was constructed to simulate the recognition of a standard MNIST data set.[56] The achieved recognition accuracy of 89% could meet the application requirements for performing the learning and recognizing tasks (Figure S36 and S37a–d, Supporting Information). Therefore, such artificial neural network could be applied to electronic textile system to process complex physiological signals like brainwaves. For instance, our textile-type memristors could distinguish signals of "Normal", "Epileptic interictal phase" and "Epileptic ictal phase" from the electroencephalogram (EEG) dataset collected from patients with epilepsy,[57] with a high recognition accuracy of 95% (Figure 5h; Figure S37e,f, Supporting Information). It is envisioned that using such real-time medical diagnosis textile system can offer timely feedback according to the patients' physiological statuses and give appropriate first aid advices to non-professionals in emergent situations (Figure 5g).

3. Conclusion

In conclusion, we present a highly reliable textile-type memristor by weaving Pt/CuZnS fiber with aligned nanochannels. It showed both ultralow set voltage and set voltage variation. The nanochannels with amorphous/crystalline heterostructures in the CuZnS layer offered confined space to promote orderly and reliable conductive Ag filaments. The textile-type memristors could seamlessly integrate with multi-functional electronic textiles/fibers to realize all-textile smart system for efficient and comfortable interactive human-machine interfaces. Our textile-type memristor open a route to develop advanced information processing devices for wearable electronics and smart textiles. For practical wearable applications, numerous efforts should be made to further improve durability under harsh service conditions and achieve high device-to-device reproducibility for large-scale array-level applications.

Supporting Information

Supporting Information is available from the Wiley Online Library or from the author.

Acknowledgements

This work was supported by the STCSM (20JC1414902 and 21511104900), the NSFC (T2222005, 22075050, 52122310, 22175042, and 22105045), and the CPSF (VLH1717003 and KLH1717015).

Conflict of Interest

The authors declare no conflict of interest.

Data Availability Statement

The data that support the findings of this study are available from the corresponding author upon reasonable request.

Keywords

all-textile integrated electronic system, electronic textile, memristors, nanochannel

Received: February 10, 2023
Revised: May 2, 2023
Published online: July 2, 2023

 © 2023 Wiley-VCH GmbH

15214095, 2023, 32, Downloaded from https://onlinelibrary.wiley.com/doi/10.1002/adma.202301321 by Fudan University, Wiley Online Library on [12/12/2024]. See the Terms and Conditions (https://onlinelibrary.wiley.com/terms-and-conditions) on Wiley Online Library for rules of use; OA articles are governed by the applicable Creative Commons License

15214095, 2023, 32, Downloaded from https://onlinelibrary.wiley.com/doi/10.1002/adma.202301321 by Fudan University, Wiley Online Library on [12/12/2024]. See the Terms and Conditions (https://onlinelibrary.wiley.com/terms-and-conditions) on Wiley Online Library for rules of use; OA articles are governed by the applicable Creative Commons License

[1] Y. Wu, S. S. Mechael, T. B. Carmichael, *Acc. Chem. Res.* **2021**, *54*, 4051.
[2] X. Xu, S. Xie, Y. Zhang, H. Peng, *Angew. Chem., Int. Ed.* **2019**, *58*, 13643.
[3] G. Chen, Y. Li, M. Bick, J. Chen, *Chem. Rev.* **2020**, *120*, 3668.
[4] J. Chang, J. Shang, Y. Sun, L. K. Ono, D. Wang, Z. Ma, Q. Huang, D. Chen, G. Liu, Y. Cui, Y. Qi, Z. Zheng, *Nat. Commun.* **2018**, *9*, 4480.
[5] L. Yin, K. N. Kim, J. Lv, F. Tehrani, M. Lin, Z. Lin, J. M. Moon, J. Ma, J. Yu, S. Xu, J. Wang, *Nat. Commun.* **2021**, *12*, 1542.
[6] B. M. Quandt, L. J. Scherer, L. F. Boesel, M. Wolf, G. L. Bona, R. M. Rossi, *Adv. Healthcare Mater.* **2015**, *4*, 330.
[7] X. Shi, Y. Zuo, P. Zhai, J. Shen, Y. Yang, Z. Gao, M. Liao, J. Wu, J. Wang, X. Xu, Q. Tong, B. Zhang, B. Wang, X. Sun, L. Zhang, Q. Pei, D. Jin, P. Chen, H. Peng, *Nature* **2021**, *591*, 240.
[8] J. Shi, S. Liu, L. Zhang, B. Yang, L. Shu, Y. Yang, M. Ren, Y. Wang, J. Chen, W. Chen, Y. Chai, X. Tao, *Adv. Mater.* **2020**, *32*, 1901958.
[9] Z. Zhou, K. Chen, X. Li, S. Zhang, Y. Wu, Y. Zhou, K. Meng, C. Sun, Q. He, W. Fan, E. Fan, Z. Lin, X. Tan, W. Deng, J. Yang, J. Chen, *Nat. Electron.* **2020**, *3*, 571.
[10] C. Wang, S. J. Liang, C. Y. Wang, Z. Z. Yang, Y. Ge, C. Pan, X. Shen, W. Wei, Y. Zhao, Z. Zhang, B. Cheng, C. Zhang, F. Miao, *Nat. Nanotechnol.* **2021**, *16*, 1079.
[11] Q. Xia, J. J. Yang, *Nat. Mater.* **2019**, *18*, 309.
[12] Y. Liu, X. Zhou, H. Yan, Z. Zhu, X. Shi, Y. Peng, L. Chen, P. Chen, H. Peng, *Adv. Funct. Mater.* **2022**, *32*, 2201510.
[13] K. Roy, A. Jaiswal, P. Panda, *Nature* **2019**, *575*, 607.
[14] Y. Li, L. Loh, S. Li, L. Chen, B. Li, M. Bosman, K. W. Ang, *Nat. Electron.* **2021**, *4*, 348.
[15] Z. Wang, H. Wu, G. W. Burr, C. S. Hwang, K. L. Wang, Q. Xia, J. J. Yang, *Nat. Rev. Mater.* **2020**, *5*, 173.
[16] K. Shibuya, R. Dittmann, S. Mi, R. Waser, *Adv. Mater.* **2010**, *22*, 411.
[17] M. Lanza, K. Zhang, M. Porti, M. Nafría, Z. Y. Shen, L. F. Liu, J. F. Kang, D. Gilmer, G. Bersuker, *Appl. Phys. Lett.* **2012**, *100*, 123508.
[18] G. Di Martino, A. Demetriadou, W. Li, D. Kos, B. Zhu, X. Wang, B. de Nijs, H. Wang, J. MacManus Driscoll, J. J. Baumberg, *Nat. Electron.* **2020**, *3*, 687.
[19] D. Kumar, R. Aluguri, U. Chand, T. Y. Tseng, *Appl. Phys. Lett.* **2017**, *110*, 203102.
[20] M. J. Lee, C. B. Lee, D. Lee, S. R. Lee, M. Chang, J. H. Hur, Y. B. Kim, C. J. Kim, D. H. Seo, S. Seo, U. I. Chung, I. K. Yoo, K. Kim, *Nat. Mater.* **2011**, *10*, 625.
[21] Y. Wang, Q. Liu, S. Long, W. Wang, Q. Wang, M. Zhang, S. Zhang, Y. Li, Q. Zuo, J. Yang, M. Liu, *Nanotechnology* **2010**, *21*, 045202.
[22] H. Yeon, P. Lin, C. Choi, S. H. Tan, Y. Park, D. Lee, J. Lee, F. Xu, B. Gao, H. Wu, H. Qian, Y. Nie, S. Kim, J. Kim, *Nat. Nanotechnol.* **2020**, *15*, 574.
[23] C. Ran, J. Xu, W. Gao, C. Huang, S. Dou, *Chem. Soc. Rev.* **2018**, *47*, 4581.
[24] Z. Zhao, A. Abdelsamie, R. Guo, S. Shi, J. Zhao, W. Lin, K. Sun, J. Wang, J. Wang, X. Yan, J. Chen, *Nano Res.* **2022**, *15*, 2682.
[25] Y. Wang, C. J. Zanelotti, X. Wang, R. Kerr, L. Jin, W. H. Kan, T. J. Dingemans, M. Forsyth, L. A. Madsen, *Nat. Mater.* **2021**, *20*, 1255.
[26] W. A. Catterall, G. Wisedchaisri, N. Zheng, *Nat. Chem. Biol.* **2017**, *13*, 455.
[27] A. E. Pereda, *Nat. Rev. Neurosci.* **2014**, *15*, 250.
[28] S. Choi, S. H. Tan, Z. Li, Y. Kim, C. Choi, P. Y. Chen, H. Yeon, S. Yu, J. Kim, *Nat. Mater.* **2018**, *17*, 335.
[29] X. Mou, J. Tang, Y. Lyu, Q. Zhang, S. Yang, F. Xu, W. Liu, M. Xu, Y. Zhou, W. Sun, Y. Zhong, B. Gao, P. Yu, H. Qian, H. Wu, *Sci. Adv.* **2021**, *7*, eabh0648.
[30] Z. Hemmat, J. Cavin, A. Ahmadiparidari, A. Ruckel, S. Rastegar, S. N. Misal, L. Majidi, K. Kumar, S. Wang, J. Guo, R. Dawood, F. Lagunas, P. Parajuli, A. T. Ngo, L. A. Curtiss, S. B. Cho, J. Cabana, R. F. Klie, R. Mishra, A. Salehi Khojin, *Adv. Mater.* **2020**, *32*, 1907041.
[31] S. W. Shin, G. L. Agawane, M. G. Gang, A. V. Moholkar, J. H. Moon, J. H. Kim, J. Y. Lee, *J. Alloys Compd.* **2012**, *526*, 25.
[32] X. Xu, J. Bullock, L. T. Schelhas, E. Z. Stutz, J. J. Fonseca, M. Hettick, V. L. Pool, K. F. Tai, M. F. Toney, X. Fang, A. Javey, L. H. Wong, J. W. Ager, *Nano Lett.* **2016**, *16*, 1925.
[33] Y. Liu, T. Tan, B. Wang, R. Zhai, X. Song, E. Li, H. Wang, H. Yan, *J. Colloid Interface Sci.* **2008**, *320*, 540.
[34] G. Hodes, *Phys. Chem. Chem. Phys.* **2007**, *9*, 2181.
[35] Y. X. Duan, F. L. Meng, K. H. Liu, S. S. Yi, S. J. Li, J. M. Yan, Q. Jiang, *Adv. Mater.* **2018**, *30*, 1706194.
[36] Y. Yang, P. Gao, S. Gaba, T. Chang, X. Pan, W. Lu, *Nat. Commun.* **2012**, *3*, 732.
[37] F. Yuan, Z. Zhang, C. Liu, F. Zhou, H. M. Yau, W. Lu, X. Qiu, H. S. P. Wong, J. Dai, Y. Chai, *ACS Nano* **2017**, *11*, 4097.
[38] J. Lee, W. D. Lu, *Adv. Mater.* **2018**, *30*, 1702770.
[39] C. Shi, J. Wang, M. L. Sushko, W. Qiu, X. Yan, X. Y. Liu, *Adv. Funct. Mater.* **2019**, *29*, 1904777.
[40] Y. Yin, J. Han, Y. Zhang, X. Zhang, P. Xu, Q. Yuan, L. Samad, X. Wang, Y. Wang, Z. Zhang, P. Zhang, X. Cao, B. Song, S. Jin, *J. Am. Chem. Soc.* **2016**, *138*, 7965.
[41] D. Li, L. Zhao, Q. Xia, J. Wang, X. Liu, H. Xu, S. Chou, *Adv. Funct. Mater.* **2022**, *32*, 2108153.
[42] S. Zhang, Q. Fan, Y. Liu, S. Xi, X. Liu, Z. Wu, J. Hao, W. K. Pang, T. Zhou, Z. Guo, *Adv. Mater.* **2020**, *32*, 2000380.
[43] L. Cai, J. He, Q. Liu, T. Yao, L. Chen, W. Yan, F. Hu, Y. Jiang, Y. Zhao, T. Hu, Z. Sun, S. Wei, *J. Am. Chem. Soc.* **2015**, *137*, 2622.
[44] X. Hao, Y. Wang, J. Zhou, Z. Cui, Y. Wang, Z. Zou, *Appl. Catal. B* **2018**, *221*, 302.
[45] J. Zhu, T. Zhang, Y. Yang, R. Huang, *Appl. Phys. Rev.* **2020**, *7*, 011312.
[46] H. Qiu, T. Xu, Z. Wang, W. Ren, H. Nan, Z. Ni, Q. Chen, S. Yuan, F. Miao, F. Song, G. Long, Y. Shi, L. Sun, J. Wang, X. Wang, *Nat. Commun.* **2013**, *4*, 2642.
[47] S. M. Hus, R. Ge, P. A. Chen, L. Liang, G. E. Donnelly, W. Ko, F. Huang, M. H. Chiang, A. P. Li, D. Akinwande, *Nat. Nanotechnol.* **2021**, *16*, 58.
[48] X. Zhang, C. Wu, Y. Lv, Y. Zhang, W. Liu, *Nano Lett.* **2022**, *22*, 7246.
[49] L. Pan, Z. Ji, X. Yi, X. Zhu, X. Chen, J. Shang, G. Liu, R. W. Li, *Adv. Funct. Mater.* **2015**, *25*, 2677.
[50] F. M. Bayat, M. Prezioso, B. Chakrabarti, H. Nili, I. Kataeva, D. Strukov, *Nat. Commun.* **2018**, *9*, 2331.
[51] M. Lanza, A. Sebastian, W. D. Lu, M. L. Gallo, M. F. Chang, D. Akinwande, F. M. Puglisi, H. N. Alshareef, M. Liu, J. B. Roldan, *Science* **2022**, *376*, eabj9979.
[52] M. I. Khan, S. Ali, A. A. Ikram, A. Bermak, *IEEE Access* **2021**, *9*, 84480.
[53] G. Pedretti, D. Ielmini, *Electronics* **2021**, *10*, 1063.
[54] S. Chen, Z. Lou, D. Chen, G. Shen, *Adv. Mater.* **2018**, *30*, 1705400.
[55] T. Fu, X. Liu, S. Fu, T. Woodard, H. Gao, D. R. Lovley, J. Yao, *Nat. Commun.* **2021**, *12*, 3351.
[56] C. Yang, D. Shang, N. Liu, E. J. Fuller, S. Agrawal, A. A. Talin, Y. Li, B. Shen, Y. Sun, *Adv. Funct. Mater.* **2018**, *28*, 1804170.
[57] H. Daoud, M. A. Bayoumi, *IEEE Trans. Biomed. Circuits Syst.* **2019**, *13*, 804.

© 2023 Wiley-VCH GmbH